

Near real-time flood detection in urban and rural areas using high resolution Synthetic Aperture Radar images

Article

Accepted Version

Mason, D. ORCID: <https://orcid.org/0000-0001-6092-6081>, Davenport, I., Neal, J., Schumann, G. and Bates, P. (2012) Near real-time flood detection in urban and rural areas using high resolution Synthetic Aperture Radar images. *IEEE Transactions on Geoscience and Remote Sensing*, 50 (8). pp. 3041-3052. ISSN 0196-2892 doi: <https://doi.org/10.1109/TGRS.2011.2178030> Available at <https://centaur.reading.ac.uk/24935/>

It is advisable to refer to the publisher's version if you intend to cite from the work. See [Guidance on citing](#).

To link to this article DOI: <http://dx.doi.org/10.1109/TGRS.2011.2178030>

Publisher: IEEE Geoscience and Remote Sensing Society

All outputs in CentAUR are protected by Intellectual Property Rights law, including copyright law. Copyright and IPR is retained by the creators or other copyright holders. Terms and conditions for use of this material are defined in the [End User Agreement](#).

www.reading.ac.uk/centaur

CentAUR

Central Archive at the University of Reading

Reading's research outputs online

Near real-time flood detection in urban and rural areas using high resolution Synthetic Aperture Radar images

David C. Mason¹, Ian J. Davenport¹, Jeffrey C. Neal², Guy J-P. Schumann²,
Paul D. Bates²

¹National Centre for Earth Observation, University of Reading, Reading RG6 6AL, UK.

²School of Geographical Sciences, University of Bristol, Bristol BS8 1SS, UK.

ABSTRACT

A near real-time flood detection algorithm giving a synoptic overview of the extent of flooding in both urban and rural areas, and capable of working during night-time and day-time even if cloud was present, could be a useful tool for operational flood relief management. The paper describes an automatic algorithm using high resolution Synthetic Aperture Radar (SAR) satellite data that builds on existing approaches, including the use of image segmentation techniques prior to object classification to cope with the very large number of pixels in these scenes. Flood detection in urban areas is guided by the flood extent derived in adjacent rural areas. The algorithm assumes that high resolution topographic height data are available for at least the urban areas of the scene, in order that a SAR simulator may be used to estimate areas of radar shadow and layover. The algorithm proved capable of detecting flooding in rural areas using TerraSAR-X with good accuracy, classifying 89% of flooded pixels correctly, with an associated false

positive rate of 6%. Of the urban water pixels visible to TerraSAR-X, 75% were correctly detected, with a false positive rate of 24%. If all urban water pixels were considered, including those in shadow and layover regions, these figures fell to 57% and 18% respectively.

Index terms: Algorithms, hydrology, image processing, simulation.

Corresponding author: D.C. Mason (dcm@mail.nerc-essc.ac.uk)

I. INTRODUCTION

Flooding is a major hazard in both rural and urban areas worldwide, and has occurred regularly in the UK in recent times. The UK floods of 2007 caused the country's largest peacetime emergency since WW2 [1]. The impact of global warming means that the probability of events of a similar scale happening in the future is increasing [2].

The Pitt Report set out to consider what lessons could be learned from the 2007 floods [3]. Among its many recommendations, the report highlighted the need to have real-time or near real-time flood visualisation tools available to enable emergency responders to react to and manage fast-moving events, and to target their limited resources at the highest-priority areas. It was felt that a simple GIS that could be effectively updated with timings, level and extent of flooding during a flood event would be a useful system to keep the emergency services informed.

A near real-time flood detection algorithm giving a synoptic overview of the extent of flooding in both urban and rural areas, and capable of working during night-time and day-time even if cloud was present, could thus be a useful tool for operational flood relief management. The latest generation of very high resolution Synthetic Aperture Radar (SAR) satellites now make such technology possible. A near real-time algorithm might allow the emergency services to view the geo-registered flood extent at very high resolution over the whole area overlaid on a base map a few hours after overpass. This could be difficult to achieve by other means.

The vast majority of a flooded area may be rural rather than urban, but it is very important to detect the urban flooding because of the increased risks and costs associated with it. Flood extent can be detected in rural floods using SARs such as ERS and ASAR, but these have too low a resolution (25m) to detect flooded streets in urban areas. However, a number of SARs with spatial resolutions as high as 3m or better have recently been launched that are capable of detecting urban flooding. They include TerraSAR-X, RADARSAT-2, and the four COSMO-SkyMed satellites. An important factor making near real-time operation possible is that accurate geo-registration can be performed rapidly. For example, the images from TerraSAR-X can be made available in geo-registered form to better than one pixel locational accuracy using precise knowledge of the orbit parameters [4].

In the absence of significant wind or rain, river flood-water generally appears dark in a SAR image because the water acts as a specular reflector. A near real-time flood detection algorithm using a split-based automatic thresholding procedure applied to multi-look single-polarisation TerraSAR-X data has been implemented at the Centre for Satellite-Based Crisis Information (ZKI) at the German Aerospace Centre (DLR) [5]. This searches for water as regions of low SAR backscatter using a region-growing iterated segmentation/classification approach, and requires minimal user intervention. A further more general automatic change detection method using Markov image modelling on irregular graphs has been developed by the same authors [6], and applied to flood detection with similar good success in rural areas. Another automatic method for rural

flood detection combining radiometric thresholding with region growing is described in [7]. A further method for rural areas is described in [8], though this requires manual intervention. A semi-automatic method for rural flood detection in multi-temporal COSMO-SkyMed data using an electromagnetic scattering model is described in [9, 10]. However, these techniques would require modification to work in urban areas containing radar shadow and layover.

A semi-automatic algorithm for the detection of floodwater in urban areas using TerraSAR-X has also been developed previously [11]. It uses the DLR SAR End-To-End simulator (SETES) in conjunction with LiDAR (Light Detection and Ranging) data to estimate regions of the image in which water would not be visible due to shadow or layover caused by buildings and taller vegetation [12], [13]. Ground will be in radar shadow if it is hidden from the radar by an adjacent intervening building. The shadowed area will appear dark, and may be misclassified as water even if it is dry. In contrast, an area of flooded ground in front of the wall of a building viewed in the range direction may be allocated to the same range bin as the wall, causing layover which generally results in a strong return, and a possible misclassification of flooded ground as unflooded. The algorithm is aimed at detecting flood extents for calibrating and validating an urban flood inundation model in an offline situation. It requires user interaction at a number of stages, including choosing training areas for water and non-water pixels, and this invariably introduces an element of delay into the production of the final product.

The objective of this paper is to build on a number of aspects of the existing algorithms, to automate the steps requiring manual interaction and to take advantage of the availability of LiDAR data in the urban area, in order to develop a near real-time algorithm that for the near real-time processing steps is almost completely automatic.

II. DESIGN CONSIDERATIONS

The algorithm design assumes that high resolution ($\sim 1\text{m}$) LiDAR data are available for at least the urban regions in the scene, in order that the SAR simulator may be run in conjunction with the LiDAR data to generate maps of radar shadow and layover in urban areas. The algorithm is therefore limited to urban regions of the globe that have been mapped using airborne LiDAR. However, in the UK most major urban areas in floodplains have now been mapped, and the same is true for many urban areas in other developed countries. It is further assumed that some form of (probably less accurate) Digital Elevation Model (DEM) is available for the adjacent rural areas also. This could be LiDAR data, but is more likely to be a lower resolution DEM constructed from map data (e.g. Ordnance Survey (O.S.) Landform Profile DEM), airborne InSAR or Shuttle SRTM data (the last being available for large areas of the globe). The reason for including a DEM is that false alarms from areas of low SAR backscatter may be generated from higher un-flooded ground (e.g. radar shadow due to trees), but these can be suppressed using a height threshold associated with the DEM.

As in [11], the approach adopted involves first detecting the flood extent in the rural areas, and then detecting it in the urban areas using a secondary algorithm guided by the rural flood extent. It is well-known in image processing that an improved classification can be achieved by segmenting an image into regions of homogeneity and then classifying them, rather than classifying each pixel independently using a per-pixel classifier. The use of segmentation techniques provides a number of advantages compared to per-pixel classification. Because of the high resolution of these SARs (up to 1m), individual regions on the ground may have high spectral variances, reducing the accuracy of per-pixel classifiers. In addition, because the segments created correlate well with real regions of the earth's surface, further object-related features such as object size, shape, texture and context may be used to improve the classification accuracy. In [11], an active contour model (snake) was used to detect homogeneous regions in the rural flood, with the snake being seeded as a thin closed contour covering the un-flooded river channel. However, snakes require manual intervention and involve substantial processing when applied to high resolution images such as TerraSAR-X. Instead, the approach used for rural flood detection in [5] and [6] is adopted, which involves segmentation and classification using the eCognition Developer software [14].

In [5] and [6], classification is performed by assigning all segmented homogeneous regions (objects) of the SAR image with mean backscatter less than a given threshold to the class 'flood'. Estimation of this threshold uses parts (tiles) of the image known to contain water, invariably contaminated by substantial quantities of non-water pixels. The threshold is estimated from a mixture of two clusters having different backscatter

characteristics using an un-mixing technique. In this case the threshold is chosen by using the fact that LiDAR data of the urban area must be available (unlike in [5], [6]), and by assuming that these data contain water regions, as will invariably be the case. The water regions will generally give no LiDAR return because they have acted as specular reflectors that have generated no backscatter at the sensor. These regions can be used as training areas for water (after filtering out high SAR backscatter from small objects such as boats). Similarly, it is possible to select non-water training pixels by searching in un-shadowed areas above the level of the flooding. A simple two-class Bayes classifier using the Probability Distribution Functions (PDFs) for water and non-water can then be used to select the threshold, assuming equal prior probabilities for both classes. This removes the need to adopt an un-mixing approach, as well as the need to select training pixels manually.

III. STUDY AREA AND DATA SET

The data set used for this study is based upon the 1-in-150-year flood that took place on the lower Severn around Tewkesbury, U.K., in July 2007. This resulted in substantial flooding of urban and rural areas, about 1500 homes in Tewkesbury being flooded. Tewkesbury lies at the confluence of the Severn, flowing in from the northwest, and the Avon, flowing in from the northeast. The peak of the flood occurred on July 22, and the river did not return to bankfull until July 31 [1].

On July 25, TerraSAR-X acquired a 3m-resolution StripMap image of the region (Fig.1), showing incredible detail of the flooded urban areas (Fig. 2). The TerraSAR-X incidence angle was 24° , and the image was multi-look ground range spatially enhanced. The HH polarisation mode chosen provided good discrimination between flooded and non-flooded regions [5], [15]. At the time of overpass, there was relatively low wind speed and no rain.

Aerial photos of the flooding were acquired on July 24 and 27 [11, 16], and these were used to validate the flood extent extracted from the TerraSAR-X image. The data set also included LiDAR data (2m resolution, 0.1m height accuracy) of the un-flooded area, with coincident LiDAR and aerial photography covering the two regions identified in Fig. 1. Rectangular region A covers the Tewkesbury urban area (2.6 x 2km), and the LiDAR data here were used to provide a Digital Surface Model (DSM), which included building and vegetation heights as well as the 'bare-earth' heights contained in a DEM. Region B covers a larger more rural area along the Severn (with north-south extent 12.3km, east-west extent 6km), and the data here were used to validate the TerraSAR-X flood extent in the rural area. In the rural areas outside rectangle A, an O.S. Landform Profile DEM generated from 1:10000 map contours [17] and having 10m spatial resolution and 2.5m height accuracy was used as an example of a lower resolution, less accurate DEM that might be employed in rural areas. Finally, the data set included O.S. Mastermap data [17] of roads, railways and embankments in the area, which would invariably be present in any simple GIS used by the emergency services.

IV. METHOD

Processing is carried out firstly within the region covered by LiDAR including the urban area (i.e. rectangle A in Fig. 1) using SAR and LiDAR data re-sampled to 1m pixel size . This re-sampling naturally does not generate any additional spatial resolution in the SAR image, but has the effect of maintaining resolution during the region-growing process ultimately performed in the urban flood detection. Processing is then carried out on a lower-resolution (2.5m pixel size) SAR image covering the whole of Fig.1 (13 x 18 km), in order to speed up processing over the larger area. The results for rectangle A in the lower resolution image are finally replaced with those obtained at higher resolution. Steps in the processing chain are shown in Fig. 3.

A. Higher resolution processing in rectangle A

Steps in the higher resolution processing chain applied to rectangle A include pre-processing operations carried out prior to image acquisition, and near real-time operations carried out after the geo-registered image has been obtained.

1) Pre-processing:

a) Delineation of urban areas: The main urban areas are delineated. Currently this process is performed manually as it is a pre-processing operation that is not time-critical.

b) Calculation of radar shadow and layover: The calculations of radar shadow and layover are performed using the LiDAR DSM [11]. Substantial areas of urban flood water may not be visible to the SAR because of the presence of radar shadow and layover due to buildings or taller vegetation. The effect is described in [11] and illustrated in Fig. 5 of [11]. In summary, sections of the image in radar shadow will appear dark in the SAR images, and may simulate water even if they are un-flooded. Other sections of ground may be subject to layover from adjacent structures such as walls, generally leading to a bright return even if the ground is flooded. The DLR SAR End to End Simulator SETES [12], [13] is used to estimate regions of the TerraSAR-X image in which water will not be visible due to the presence of shadow or layover. The estimation of these regions is purely geometrical, and uses the LiDAR DSM of the scene's surface as well as the radar flight trajectory and incidence angle. Due to the fact that only boolean information is required describing whether or not a pixel is affected by layover or shadow, no simulation of realistic backscattering values is necessary. The binary images for shadow and layover are combined to form a single image showing the shadow and layover regions (Fig. 4). In Fig. 4, TerraSAR-X is travelling approximately North-South and looking West. It can be seen that most shadow and layover occurs in streets parallel to the satellite direction of travel, whereas streets perpendicular to this have less shadow/layover.

c) Construction of compound DEM: A compound DEM is constructed for rectangle A, being the DSM in the urban areas and the DEM in the rural areas of the rectangle. In the rural areas, building and vegetation heights are removed from the DSM to form the DEM

using the processing algorithm of the Environment Agency of England and Wales (EA) [18]. The compound DEM is required because different processing is applied in the urban and rural areas of rectangle A. The slope of the DEM is also calculated in the rural areas.

d) Identification of high land height threshold: In order to identify a set of pixels in regions of high land that potentially contain no water, the height (h_h) above which lie 10% of pixels in the rural DEM is calculated.

e) Segmentation of shadow/layover: The shadow/layover objects are segmented using the multi-resolution segmentation algorithm of the eCognition Developer software [14]. This algorithm is used at several stages in the processing, and is based on the Fractal Net Evolution concept of [19]. This employs an iterated bottom-up segmentation technique based on pair-wise merging of adjacent regions. The merging is governed by a local mutual best fitting algorithm, which aims to achieve the lowest increase in object heterogeneity by merging the two adjacent regions separated by the smallest distance in a feature space determined by mean spectral and textural features. The maximum allowable heterogeneity of the objects is set by a user-defined scale parameter, homogeneity criterion h , which is comprised of object spectral homogeneity h_c and shape homogeneity h_s ($h_c + h_s = 100\%$), with h_s in turn being made up of object compactness $h_{compact}$ and object smoothness h_{smooth} ($h_{compact} + h_{smooth} = 100\%$). The larger the scale parameter is, the larger are the image objects. As the segmentation of the shadow/layover objects is applied to the simple binary shadow/layover image (Fig. 4), the default settings of the scale parameters are used ($h = 10$, $h_s = 10\%$, $h_{compact} = 10\%$,). Objects in shadow or

layover (i.e. dark in Fig. 4) are assigned to the shadow/layover class, while all other objects are set unclassified.

f) Segmentation of potential water and high land: The unclassified objects in the above segmentation are further segmented by applying the multi-resolution segmentation algorithm to the compound LiDAR DEM, again using the default scale settings. Regions containing water in the DEM will have unassigned heights, and will be represented as individual objects in the segmentation. These are classified as potential water objects. At the same time, objects having mean heights above that for high land (h_h), that do not contain unassigned heights (so that they are not water), and are not in shadow/layover regions (so that they do not contain shadow having similar low backscatter to water), are classed as high land.

2) *Near Real-time Processing:*

g) Speckle filtering of SAR sub-image: Near real-time processing may begin as soon as the multi-look geo-registered TerraSAR-X image becomes available. Following [5], this is first speckle-filtered using adaptive filtering to reduce salt-and-paper noise using the Gamma-MAP filter of [20] with a window size of 3 x 3 pixels. The speckle-filtered data are used for processing in the rural areas, though in the urban areas the original SAR data are employed instead to maintain spatial resolution.

h) Identification of water and high land objects: The objects classed as potential water and high land in the multi-resolution segmentation produced during step (f) of pre-processing are segmented further using the speckle-filtered SAR image. The segmentation scale parameters were set by a process of trial-and-error based on visual interpretation of the segmentation results, in order to produce objects such as fields corresponding to those visible in the SAR image. No special interpretation skills were required in this process. It was found that good results could be obtained using a large scale parameter ($h = 100$), coupled with a larger shape homogeneity ($h_s = 40\%$) and larger compactness ($h_{compact} = 40\%$) than the default settings, in order to select for compact objects that were not over-segmented. These parameters were used in this and subsequent multi-resolution segmentations in the processing chain, and are viewed as constants that do not need to be reset by the user, at least for this SAR data type. The ‘potential water’ objects should be largely made up of water regions contaminated with objects such as boats. Segmented water objects should have a relatively large area and low mean intensity, while objects such as boats should have small area and high mean intensity. An uncontaminated set of water objects could be obtained by selecting ‘potential water’ objects having areas greater than 180 m^2 and mean intensities less than 100 DN units.

i) Calculation of mean SAR backscatter threshold: The mean intensity threshold that best separates water objects from non-water objects is calculated. For the water objects, a histogram of pixel intensities is constructed by weighting the mean intensity of each object by its area (note that this is not the same as constructing the histogram from the

intensities of the pixels making up the water objects). A similar histogram is constructed from the area-weighted mean intensities of the high land objects (assumed to be an uncontaminated sample of non-water objects). Both histograms are normalised to assume equal prior probabilities for each class. The threshold T giving the minimum misclassification of water and non-water objects is calculated from the measured histograms. From Fig. 5, the minimum error rate is obtained using a threshold T of 57 DN units. This approach takes into account the fact that objects are being classified rather than the individual pixels making up the objects.

j) Flood detection in rural areas of rectangle A: This step begins with the segmentation produced in step (f), containing shadow/layover, potential water and high land objects. Potential water and high land objects are reclassified as unclassified, and adjacent unclassified objects are merged together to reduce the number of objects. The unclassified objects are then segmented further using the speckle-filtered SAR image, employing multi-resolution segmentation using the scale parameters of step (h). All resulting objects with a mean SAR backscatter intensity less than or equal to the threshold T are classed as 'flood'. This step classifies the majority of the flooded area in rectangle A.

k) Calculation of local waterline height threshold map: As a precursor to flood detection in urban areas, a local waterline height threshold map is calculated using the initial flood map derived in the previous step. It seems reasonable to assume that water in the urban areas should not be at a substantially higher level than that in the nearby rural areas.

Unless there is significant ponding (for example, on the falling limb of the hydrograph), there should be very little water at higher urban levels. However, unless a height threshold is imposed, there could be a substantial false positive rate of water at these levels, as shown in [11]. The spatial variability of this threshold reflects the fact that different parts of the area can be flooded to different heights. For example, the waterline height along the river Severn in the northwest of rectangle A was 0.5m higher than that along smaller tributaries in the southeast [11]. The method detects local flood waterline heights in regions of low DEM slope within a range of $\pm 1.5\text{m}$ of the mean water height, and interpolates these heights over rectangle A. Rectangle A is divided into four quadrants, each of size 1.3 x 1km. Within each quadrant, waterlines are detected by applying the Sobel edge detector to the binary flood map. Because the flood map has errors at this stage, edges will be present at the true waterlines, but also in the interior of the water objects due to regions of emergent vegetation and shadow/layover regions (because these have been segmented out), as well as above the waterline due to higher water alarms. To increase the signal-to-noise ratio of true edges, a dilation and erosion operation is performed on the water objects to eliminate some of the artefacts prior to finding edges. Water objects are first dilated by 40 pixels, then eroded by the same amount. It is required that an edge pixel is present at the same location before and after dilation and erosion. This tends to select for true waterline segments on straighter sections of exterior boundaries of water objects. To suppress false alarms further, waterline heights in regions of low DEM slope within $\pm 1.5\text{m}$ of the mean water height are selected. The slope threshold must be set quite high (0.25), because in a valley-filling event the waterlines may be on moderate rather than shallow slopes. In order to find the

mean waterline height in the quadrant, a histogram is constructed of the waterline heights, and the positions of the histogram maxima are found, including that of the main maximum. Generally, the mean waterline height in the quadrant is set to correspond to the height of the main maximum. However, if any substantial maxima greater than half that of the main maximum is present at a higher height, the highest of these is chosen instead. This latter rule copes with the situation where a substantial number of erroneous low waterline heights in the interior of water objects have not been eliminated. Fig. 6 shows the histograms for the NW and SE quadrants of rectangle A (see Fig. 2), together with the mean waterline heights calculated. The local mean waterline heights in the four quadrants are interpolated to a height threshold image using bilinear interpolation. A guard height threshold of 0.3 m is added to this image to allow a height tolerance. If it was required to detect local mean water line heights in an urban area of different size to rectangle A, the method should divide the area into non-overlapping tiles of area about 1km^2 , so that sufficient waterline heights would be available to construct a sensible histogram in each tile.

l) Rural flood refinement: The segmentation of the rural flood generated in step (j) is then refined. Shadow/layover objects in the rural areas are often adjacent to rows of trees along field boundaries, which are likely to be flooded if they are adjacent to flood objects. As a result, shadow/layover objects in rural areas with a relative border to flood ≥ 0.3 are reclassified as flooded, iterating until no further changes occur. The relative border of an object is the ratio of its shared border length with flood objects to its total border length. In a similar manner, unclassified objects in rural areas that are long and

thin and adjacent to flood objects are often hedgerows that are likely to be flooded even though emergent. Provided such objects have a relative border to flood ≥ 0.5 , do not lie along a road, railway or embankment, and have either a length/width ratio ≥ 2 or a compactness ≥ 2 , they are reclassified as flooded. The compactness of an object is the product of its length and width divided by its area, and the compactness criterion is included because in some cases hedgerows along two perpendicular field boundaries join to form an L-shaped object with low length/width ratio but high compactness. The thresholds above were determined experimentally, though results were not overly sensitive to them. These rules for shadow/layover and unclassified objects proved more effective than a rule requiring that the mean height of such objects be less than or equal to that of the adjacent flood objects.

While flood-water usually appears dark compared to the surrounding un-flooded land because of specular reflection from the smooth water surface, wind or rain may cause roughening of the water such that the backscatter from it may rise to similar or greater levels than the surrounding land. Emergent vegetation may also produce increased backscatter. Because different parts of the flooded reach may have different exposures to wind, rain and emergent vegetation, it is unlikely that a single mean SAR backscatter intensity threshold will be appropriate for all flood objects along the reach. It would be possible to perform a second iteration of the segmentation/classification scheme, segmenting with a smaller scale factor and the same intensity threshold [5], but this would tend to split an object exposed to wind into smaller dark and light objects, whereas in fact the original large scale segmentation of the object may be correct but the object is

merely textured. This problem did not appear to be particularly widespread, and as a result a simple rule was introduced to the effect that an unclassified object with a relative border to flood ≥ 0.3 and mean SAR backscatter intensity $\leq T'$ (where $T' = 1.1T$) is reclassified as flooded. This rule is iterated until no further change occurs.

Although this rule may misclassify some un-flooded objects as flooded, these as well as others are subsequently largely reclassified by setting unclassified any flood objects having mean heights above the waterline height threshold. Furthermore, if any pixels comprising a flood object have heights above this threshold, they are set unclassified. This identifies the final rural flood classification in rectangle A.

m) Flood detection in urban areas of rectangle A: Flood detection in urban areas is performed by a similar approach to that described in [11], whereby, following flood delineation in rural areas, flood delineation in adjacent urban areas is performed using a simpler region-growing technique. The two methods are linked because the simpler one is initialised using knowledge of the waterline heights in the rural areas. The urban region-growing algorithm is of necessity different from the rural one, because it has been found that the PDF of pixels in flooded urban streets has a substantial tail towards higher backscatter values compared to the PDF of rural water pixels [11]. This appears to be caused by high backscatter from street furniture (cars, etc) as well as inaccuracies in the layover calculation caused by the limited resolution of the LiDAR. In order to maintain spatial resolution in urban areas, the original multi-look SAR data rather than the speckle-filtered data are used at this stage. A set of seed regions having low backscatter is

identified in the urban areas using training data to classify pixels into urban water and non-water classes. Training areas for water are provided by the river water objects identified in step (h). Training areas for urban pixels not containing water are taken from the high land objects identified in step (h). A Bayesian classification is performed assuming equal prior probabilities for each class [21] i.e.

$$\text{if } P(\omega_1 / g) > P(\omega_2 / g) \text{ classify } g \text{ as } \omega_1, \text{ else as } \omega_2 \quad (1)$$

where $P(\omega_i / g)$ is the posterior probability of a pixel with DN value g being from class ω_i , where $\omega_1 = \text{water}$ and $\omega_2 = \text{non-water}$. Note that, in this case, pixels are being classified individually rather than as objects, so that the minimum error rate can be obtained directly from the Bayes rule. The minimum error rate was obtained with a threshold (T_u) of 68 DN units (Fig. 7).

Unclassified pixels in the urban area are then classified as water seeds if they have SAR backscatter less than T_u , heights that are less than the spatially varying waterline height threshold map calculated in step (k), and do not lie in shadow/layover areas. In [11], it was found that that seed pixels from the same body of urban water were generally close together, though not always connected. Seed pixels from different bodies of urban water were generally much farther apart. Seed pixels are therefore clustered together using a region growing approach involving iterated 8-neighbour pixel dilation and 8-neighbour connected component labelling [22]. Clustering is carried out on the basis of distance of a pixel to the nearest seed pixel rather than similarity between the DN values of pixel and seed. At each iteration, seed regions are dilated by a pixel, then the number of connected

regions is found. In the dilation process, the re-sampling described in Section IV ensures that at each iteration only a 1m-wide border is added to a region, maintaining the shape of the region better than if pixels at the SAR resolution (3m) had been added. Ideally dilation should continue until all pixels from the same water body are agglomerated into that body, but none of the different water bodies are fused together. In practice, iteration is terminated after five iterations, when the number of connected regions began to show relatively little change. At this point regions are eroded by the total amount by which they have been dilated.

n) Urban flood refinement: The urban flood classification map output from step (m) is included in the segmentation available at the end of the rural flood refinement (step l), by performing a multi-resolution segmentation to refine the unclassified urban areas of this segmentation to match the urban flooding, and classifying these objects as urban flood. An attempt is then made to grow the urban flood objects where possible by merging with them unclassified or shadow/layover objects bordering them and of lower or similar height. It is first necessary to break up those shadow/layover objects having parts lying above and other parts lying below the waterline height threshold map where necessary, by performing a multi-resolution segmentation using the threshold map. Then unclassified or shadow/layover objects in the urban area with mean heights less than the height threshold map and with a relative border to urban flood ≥ 0.3 , are classified as urban flood provided that the mean height of the object is less than or equal to the mean height of the adjacent urban flood objects. This identifies the final urban flood classification in rectangle A.

B. Lower resolution processing over the whole image

Processing of the whole image at lower resolution follows a similar flow path to that used for rural flood classification in rectangle A. However, the pre-processing operations carried out on the higher resolution image, such as the shadow/layover calculation, are unnecessary at this stage, and all processing steps are near real-time.

o) SAR image speckle filtering: The whole image is speckle-filtered using the method of step (g).

p) Flood detection: The speckle-filtered SAR image is segmented using a multi-resolution segmentation employing the scale parameters of step (h). The mean SAR backscatter intensity threshold calculated in step (i) is then used to classify the image objects. All objects with a mean intensity less than or equal to the threshold T are classed as flood. It is valid to apply the same threshold T used in rural areas of rectangle A to the whole image, because there is no reason to suppose that the mean SAR backscatter of flood objects should have different distributions in the two cases. As with rectangle A, this step classifies the majority of the flooded area in the whole image.

q) Calculation of waterline height threshold: Only a crude global waterline height threshold could be set at this stage because of the low height accuracy of the O.S. Landform Profile DEM compared to the LiDAR DEM. Although the quoted height accuracy is $\pm 2.5\text{m}$, experiments indicated that it was best to set the threshold

conservatively, and a threshold of 25m (about 10m above the highest point on the riverbank along the reach) was employed. The simplistic approach adopted for this threshold setting means that it could be set during pre-processing.

r) Flood refinement: The flood segmentation is refined in a similar manner to that used in step (l). As the whole area is predominantly rural, unclassified objects that are long and thin and adjacent to flood objects are often hedgerows that are likely to be flooded even though emergent. Provided such objects have a relative border to flood ≥ 0.5 , do not lie along a road, railway or embankment, and have either a length/width ratio ≥ 2 or a compactness ≥ 2 , they are reclassified as flooded. To cope with the fact that a single mean SAR intensity threshold is inappropriate for all flood objects along the reach, the simple rule of step (l) is again used whereby an unclassified object with a relative border to flood ≥ 0.3 and mean SAR backscatter intensity $\leq T'$ (where $T' = 1.1T$) is reclassified as flooded, this procedure being iterated until no further change occurs. As in step (l), flood objects having mean heights above the waterline height threshold of step (q), or any pixels comprising a flood object having heights above this threshold, are set unclassified.

s) Merging of lower and higher resolution classification images: The results for rectangle A in the lower resolution image are replaced with those obtained at higher resolution, though only in the rural areas of rectangle A. This identifies the final flood classification over the whole image.

V. PROCESSING OF THE VALIDATION DATA

Validation of the flood extents in regions A and B was carried out using aerial photograph mosaics acquired approximately 19 hours before and 53 hours after the satellite overpass. The method used is described in [11]. For each mosaic, a uniformly-distributed set of flood extent waterline points in areas of low slope were selected manually and heighted using the LiDAR data. These heights were interpolated to form a water height threshold map over the whole area covered by the aerial photos using kriging. Areas in the LiDAR images below the local height threshold were classed as water. A height threshold map for the overpass time was then constructed using linear interpolation between the two aerial photo height threshold maps, and areas in the LiDAR images below the local height threshold were taken as the flood extent at overpass time. Some minor editing of this was necessary to correct obvious errors compared to the aerial photos acquired 19 hours prior to overpass. The aerial photo flood extents in regions A and B derived in this manner were assumed to be error-free for the purposes of validation.

VI. VALIDATION OF THE TERRASAR-X FLOOD EXTENT

The flood extent estimated by TerraSAR-X in the urban and rural areas was validated using the flood extent estimated from the aerial photographs. Results are considered separately for the urban and rural areas.

A. Urban flood classification accuracy

The accuracy of the basic urban flood detection algorithm (step (m)) is first considered. Of the urban water pixels in rectangle A, 75% were correctly detected by TerraSAR-X, giving a false negative rate of 25%. The associated false positive rate of urban non-water pixels incorrectly classified as water was 24% (table 1). Fig. 8 shows the correspondence between the aerial photograph and TerraSAR-X flood extents that was achieved in the main urban areas of Tewkesbury, superimposed on the LiDAR image (from which all but the main urban areas have been masked out).

These figures quantify the fraction of the urban flood extent that is visible to TerraSAR-X and also detected by it. However, it is more pertinent to consider the fraction of the urban flood extent that is visible in the aerial photos that is detected by TerraSAR-X. This fraction will be lower because flooded pixels in the shadow/layover regions must now be included. If this was done, only 57% of the urban water pixels were now detected by TerraSAR-X, with a false positive rate of 18%. It can be seen that the classification obtained in the urban area is of limited accuracy, partly because of TerraSAR-X's poor visibility of the ground surface due to shadow and layover.

The basic urban flood detection step (m) is followed by the urban flood refinement step (n), and the effect of this was measured. Shadow/layover regions are implicitly included at this stage, in an attempt to grow urban flood objects where possible by merging them with unclassified or shadow/layover objects bordering them and of lower or similar

height. There was a small increase in the urban water detection rate to 59%, but this was offset by an increase in the false positive rate to 26%. As a result, there seems to be no advantage in applying the urban flood refinement step in this case. This may be due to the limited resolution of the LiDAR data used in the shadow/layover calculation, and step (n) may prove more useful if higher-resolution LiDAR data became available.

The effect of using speckle-filtered rather than original SAR data in this step was also quantified. It was first necessary to calculate the SAR backscatter threshold giving the minimum error rate for the speckle-filtered SAR data in an analogous fashion to that carried out in step (m). The revised SAR threshold was calculated to be 55 DN units. Using this, and including flooded pixels in the shadow/layover regions, only 35% of urban water pixels were correctly detected, with an associated false positive rate of 7%. This detection rate was considerably lower than that obtained using the original SAR data (57%), though the false positive rate was also lower. The total misclassification rate using speckle-filtered data was 72%, compared to 61% using the original SAR data, thus justifying the use of original data in this step.

B. Rural flood classification accuracy

The accuracy of flood detection in rural areas was primarily assessed using the aerial photo validation data of region B. 89% of the water pixels in region B were correctly detected by TerraSAR-X, giving a false negative rate of 11%. The associated false positive rate was 6%. Fig. 9 shows the correspondence between the aerial photograph and

TerraSAR-X flood extents that was achieved in region B, superimposed on the TerraSAR-X image.

The effect of the coarse DEM on the classification could not be reliably assessed using the validation data in region B, as very little of region B was above the coarse DEM waterline height threshold of 25m. However, over the whole image, the total number of flood pixels set unclassified because they were above this threshold was only 1.4%, so that, even assuming that these were all false alarms, the effect of the coarse DEM appeared small.

The accuracy of flood detection in the rural area of rectangle A was 97%, giving a false negative rate of 3%. The associated false positive rate was 21%, due partly to the misclassification of a field that was only just flooded in the aerial photos being classed as un-flooded in the TerraSAR-X image. However, the rural area in rectangle A is only a small fraction (less than 10%) of that in region B.

VII. OPERATIONAL CONSIDERATIONS

In order to obtain a high resolution satellite SAR image of a developing flood, it would be necessary immediately after a storm forecast had been issued to initiate operations similar to those involved in an invocation of the International Charter “Space and Major Disasters” [23]. When the Charter is invoked, Space Agencies around the world direct their satellites to image the flooding if possible. Current practice usually involves waiting

until the disaster has developed somewhat before initiating the imaging, but this would need to be modified to invoke imaging immediately after the storm forecast had been issued. ESA's Heterogeneous Mission Accessibility (HMA) project [24], which aims to allow seamless access to data from multiple earth observation missions, is likely to have a role to play in this process.

In order to ensure that a SAR image was obtained in near real-time, it would be necessary to minimise the time delay between an overpass and the production of the resulting SAR flood extent. The pre-processing operations could be carried out in parallel with tasking the satellite to acquire the image of flooding. Considering TerraSAR-X as an example, TerraSAR-X allows satellite tasking twice a day, so that the shadow/layover map could be generated prior to the image acquisition by running SETES on the LiDAR data given the SAR trajectory and proposed look angle. The DEM and vegetation height map could be generated off-line at an earlier date, and retrieved between satellite tasking and image acquisition. Download of the image to the ground station, followed by near real-time processing of the raw SAR to a multi-look image, automatic geo-registration and delineation of the flood extent, could in theory be carried out within a few hours after overpass. For example, it is known that raw TerraSAR-X images of the UK can be downloaded to the ground station, processed to multi-look images, and geo-registered to Enhanced Ellipsoid Corrected (EEC) form ready for download to the user in about 4 hours, though this facility would currently only appear to be available to scientific users of TerraSAR-X data. A blueprint of the operational system required for near real-time supply of geo-located high resolution SAR data to users is provided by the FAIRE system

developed at ESA-ESRIN, which is able to provide users with processed ENVISAT ASAR and ERS-2 SAR images approximately 3 hours after acquisition [25-27]. As far as is known, such a system has still to be developed for high resolution SAR images.

Table 2 gives the times of the various near real-time processing steps in the flood delineation run on a 3GHz desktop PC. The overall time of 19.1 minutes for this image size (6750 x 6000 pixels) could be significantly reduced using additional eCognition processing nodes [14]. In the pre-processing steps, the computing time would be dominated by the time taken to run the SAR simulator SETES on the LiDAR DSM, which for this DSM size would be about 5 minutes, a figure which may also be reduced using parallel processing (R. Speck, personal communication).

VIII. DISCUSSION

Fig. 10 shows a possible multi-scale visualisation of the flood extents in the rural and urban areas, assuming the normal situation where aerial photo data for validation are not available. Flooding is shown in blue in the rural area and in yellow in the urban area. Regions coloured brown in the urban area are areas of shadow/layover that are below the waterline height threshold, and therefore may or may not be flooded, as effectively they cannot be imaged by TerraSAR-X. It is assumed that shadow/layover regions above the height threshold are not flooded. Urban flood refinement (step n) has not been employed in generating Fig. 10.

Although developed using TerraSAR-X data, it is likely that the algorithm would also be applicable to data from other high resolution single-polarisation SARs. In this case, certain quantities treated as constants for TerraSAR-X data may need to be reset for the new data type, as data grey value ranges and speckle may differ between different sensors. In particular, the scale parameter h used in multi-resolution segmentation of SAR data, and the mean intensity threshold for potential water objects, may prove data-dependent. The thresholds used in steps (l) and (r) to identify hedgerows are geometrical quantities, and should remain valid for other sensors provided that these have similar resolution to TerraSAR-X.

The algorithm used for detecting flooding in rural areas, while based on that of [5], differs in some important respects. It is most similar to the initial large-scale segmentation and thresholding stage of [5] (see section 3.4.1 of [5]), though different values for parameters h , h_s and $h_{compact}$ have been used. The subsequent stages involving segmentation and classification of objects at medium and then small scale have not been employed. Partly this has been done to avoid the substantial computation involved in these stages for little reduction in overall error rate, and partly because a different approach has been adopted for rural flood refinement, involving a raising of the threshold to classify wind-roughened water correctly (see step (l)). From the results presented, the algorithm of [5] would appear to be somewhat more accurate than that developed here. However, an objective comparison of the two algorithms was not possible. This study used a different test area to that used in [5], as LiDAR data were available in rectangle B to aid the processing of the aerial photography (see section V). Also, different aerial

photography was used for validation in the two studies, and this was processed differently. Nevertheless, the overall algorithm presented here has the clear advantage over others that it is able to perform near real-time detection not just of rural flooding, but more importantly of urban flooding also, even if the urban flood detection accuracy obtained is limited due to radar shadow and layover.

The approach that has been adopted for detecting flood extent involves first detecting flooding in the rural areas, and then detecting it in the urban areas using a secondary algorithm guided by the rural flood extent. It should be noted that, as a result, the method will not work in a situation where a flood is totally contained within an urban area.

Because of the time delay involved in downloading the SAR data and processing the image to extract the flood extent, the image represents the flood situation a few hours previously rather than the current situation. An alternative method of using the information in the image that avoids this limitation would be to use it in conjunction with a hydraulic model of river flood flow. The flood waterline from the image could be intersected with the LiDAR DEM to obtain water surface elevations along the waterline, and these could be assimilated into the model run, correcting the water surface elevations predicted by the model where necessary [28]. This would help to keep the model ‘on track’, so that the model’s prediction of the current flood extent could be viewed with more confidence. The model would also predict water surface elevations within the shadow/layover regions.

IX. CONCLUSION

An automatic near real-time flood delineation algorithm has been developed that is capable of detecting flooding in rural areas with good accuracy, and in urban areas with reasonable accuracy. While good classification accuracy was obtained in rural areas, the accuracy was reduced in urban areas partly because of TerraSAR-X's poor visibility of the ground surface due to shadow and layover. The operational requirements for acquiring a high resolution satellite SAR image of a developing flood and determining the resulting SAR flood extent in near real-time were also considered, and it was concluded that, while technically feasible, appropriate systems for general users still have to be developed for high resolution SAR images. A limitation of this work is that it is based on data from a single flood event. Even though the scene involved contains a large area with many example situations, the algorithm needs to be tested further using other events. The method of suppressing false alarms in the urban flood delineation using a spatially distributed height threshold could be improved, and the effect of increased spatial resolution in the urban area could be studied.

ACKNOWLEDGMENT

This project was funded under NERC grant NE/I000658/1, and the UK Flood Risk Management Research Consortium (FRMRC) programme (EPSRC grant EP/F020511/1). The authors are grateful to the EA for provision of the LiDAR data, and the NERC Flood Risk from Extreme Events (FREE) programme for funding the acquisition of the aerial

photos. Thanks are also due to the referees, whose comments considerably improved the manuscript.

REFERENCES

[1] A. Stuart-Menteth. *UK Summer 2007 Floods*. Newark, CA: Risk Management Solutions, 2007.

[2] R.P. Allan and B.J. Soden, “Atmospheric warming and the amplification of precipitation extremes,” *Science*, vol. 321, no. 5895, pp.1481-1484, doi:10.1126/science.1160787, 2008.

[3] M. Pitt, “Learning lessons from the 2007 floods,” U.K. Cabinet Office Report, June 2008. Available: <http://archive.cabinetoffice.gov.uk/pittreview/thepittreview.html>.

[4] A. Schubert, M. Jehle, D. Small and E. Meier, “Influence of atmospheric path delay on the absolute geolocation accuracy of TerraSAR-X high-resolution products,” *IEEE Trans. Geoscience Rem. Sens.*, vol. 48, no. 2, pp. 751-758, 2010.

[5] S. Martinis, A. Twele and S. Voigt, “Towards operational near real-time flood detection using a split-based automatic thresholding procedure on high resolution TerraSAR-X data,” *Natural Hazards and Earth System Sciences*, vol. 9, pp. 303-314, 2009.

- [6] S. Martinis, A. Twele and S. Voigt, "Unsupervised extraction of flood-induced backscatter changes in SAR data using Markov image modeling on irregular graphs," *IEEE. Trans. Geoscience Rem. Sens.*, vol. 49, no. 1, pp. 251-263, 2011.
- [7]. P. Matgen, R. Hostache, G.J-P. Schumann, L. Pfister, L. Hoffmann and H.H.G. Savenjie, "Towards an automated SAR-based flood monitoring system: Lessons learned from two case studies." *Physics and Chemistry of the Earth*, vol. 36. no. 7-8, pp. 241-252, 2011.
- [8] V. Herrera-Cruz and F. Koudogbo, "TerraSAR-X rapid mapping for flood events." *Proc. ISPRS Workshop on High-Resolution Earth Imaging for Geospatial Information*, Hannover, 2009.
- [9] L. Pulvirenti, M. Chini, N. Pierdicci, L. Guerriero and P. Ferrazzoli, "Flood monitoring using multi-temporal COSMO-SkyMed data: image segmentation and signature interpretation," *Remote Sensing of Environment* , vol. 115, no. 4, pp. 990-1002, 2011.
- [10] L. Pulvirenti, N. Pierdicca, M. Chini and L. Guerriero, "An algorithm for operational flood mapping from Synthetic Aperture Radar (SAR) data using fuzzy logic," *Natural Hazards and Earth System Sciences*, vol. 11, no. 2, pp. 529-540, 2011.

- [11] D.C. Mason, R. Speck, B. Devereux, G.J-P. Schumann, J.C. Neal and P.D. Bates, “Flood detection in urban areas using TerraSAR-X,” *IEEE. Trans. Geoscience Rem. Sens.*, vol. 48, no. 2, pp. 882-894, 2010.
- [12] R. Speck, M. Hager, M. Garcia and H. Süß, “An end-to-end simulator for spaceborne SAR systems,” *Proc. European Conference on Synthetic Aperture Radar (Eusar)*, Cologne, 4-6 June 2002, VDE Verlag GmbH, ISBN 3-8007-2697-1, 2002.
- [13] R. Speck, P. Turchi and H. Süß, “An end-to-end simulator for high-resolution spaceborne SAR systems,” *Proc. SPIE Defense and Security*, vol. 6568, 2007.
- [14] Definiens AG, Definiens Developer 8 User Guide, Document Version 1.2.0, Munich, Germany, 2009.
- [15] J.B Henry, P. Chastanet, K. Fellah and Y.L. Desnos, “ENVISAT multi-polarised ASAR data for flood mapping,” *Int. J. Remote Sensing*, vol. 27, pp. 1921-1929, 2006.
- [16] G.J-P. Schumann, J.C. Neal, D.C. Mason and P.D. Bates, “The accuracy of sequential aerial photography and SAR data for observing urban flood dynamics, a case study of the UK summer 2007 floods,” *Remote Sensing of the Environment*, vol. 115, no. 10, pp. 2536-2546, 2011.

- [17] Ordnance Survey. (2011). Ordnance Survey Mastermap. Available:
<http://www.ordnancesurvey.co.uk/oswebsite/products/os-mastermap/>
- [18] D.C. Mason, G.J-P. Schumann and P.D. Bates, "Data utilization in flood inundation modelling." In *Flood Risk Science and Management* (eds. Pender G and Faulkner H), Wylie-Blackwell, pp. 211-233, 2011.
- [19] M. Baatz and A. Schape, "Object-oriented and multi-scale image analysis in semantic networks," *Proc 2nd Int. Symp. on Operationalization of Remote Sensing*, Enschede, Netherlands, 16-20 August 1999.
- [20] A. Lopes, E. Nezry, R. Touzi and H. Laur, "Maximum A Posteriori speckle filtering and first order texture models in SAR images," International Geo-Science and Remote Sensing Symposium (IGARSS), 24-28 May 1990, Maryland, USA, pp. 2409-2412.
- [21] R.O. Duda and P.E. Hart, "*Pattern classification and scene analysis*," Wiley, New York, 1973.
- [22] R. Adams and L. Bischof, "Seeded region growing," *IEEE Trans. Pattern Analysis and Machine Intelligence*, vol. 16, no. 6, pp. 641-647, 1994.
- [23] Charter on cooperation to achieve the coordinated use of space facilities in the event of natural or technological disasters Rev.3(25/4/2000).2. Available:
<http://www.disasterscharter.org/>

[24] European Space Agency. (2007). Heterogeneous Mission Accessibility project overview. Available: earth.esa.int/hma/

[25] R. Cossu, E. Schoepfer, Ph. Bally and L.Fusco, “Near real-time SAR based processing to support flood monitoring,” *J. Real-Time Image Processing*, vol. 4, no. 3, pp. 205-218, 2009.

[26] R. Cossu, Ph. Bally, O. Colin and L.Fusco, “Rapid mapping of flood events through the use of FAIRE,” Proc. 6th Workshop on Remote Sensing for Disaster Management Applications, Pavia, Italy, 11-12 September, 2008.

[27] R. Cossu, Ph. Bally, O. Colin and L.Fusco, “ESA Grid Processing on Demand for fast access to earth observation data and rapid mapping of flood events,” European Geosciences Union General Assembly, 2008, Vienna, Austria, 13-18 April 2008.

[28] J.C. Neal, G.J-P. Schumann, P.D. Bates and D.C. Mason, “Estimating river discharge with hydraulic models and remote sensing,” *J. Hydrology* (submitted).

Tables

Speckle-filtered SAR?	Shadow/layover masked out in aerial photos?	Urban flood refinement?	% of urban water pixels correctly classified	% false negatives	% false positives
No	Yes	No	75	25	24
No	No	No	57	43	18
No	No	Yes	59	41	26
Yes	No	No	35	65	7

Table 1. Accuracy of urban water detection.

Operation	Time (mins)
<i>Higher resolution</i>	
SAR sub-image speckle filtering	0.2
Identification of water and high land objects	1.5
Calculation of mean SAR backscatter threshold	0.1
Flood detection in rural areas of rectangle A	1.7
Calculation of local waterline height threshold map	0.5
Rural flood refinement	0.1
Flood detection in urban areas of rectangle A	0.2
Urban flood refinement	2.5
<i>Lower resolution</i>	
SAR image speckle filtering	2.0
Flood detection	10.0
Flood refinement	0.1
Merging of lower and higher resolution images	0.1
Total	19.1

Table 2. Timings of near real-time processing operations.

Figure captions

1. TerraSAR-X image of the lower Severn/Avon July 2007 flood (dark areas are water) (© DLR 2007). Rectangle A includes the urban area of Tewkesbury, and region B the rural validation area.
2. TerraSAR-X image showing detail in the urban areas of Tewkesbury (2.6 x 2 km) (© DLR 2007).
3. Steps in the processing chain.
4. Regions (black) unseen by TerraSAR-X in the LiDAR DSM due to combined shadow and layover (after [11]).
5. Variation of misclassified water and non-water objects with object mean intensity threshold T .
6. Histograms of selected waterline heights for the NW and SE quadrants of rectangle A (see Fig. 2). The upper histogram peak is at 11.8m for the NW quadrant, and 11.4m for the SE quadrant.
7. Variation of misclassified water and non-water pixels with pixel intensity threshold T_u .

8. Correspondence between the TerraSAR-X and aerial photograph flood extents in main urban areas of Tewkesbury, superimposed on the LiDAR image (yellow = wet in SAR and aerial photos, red = wet in SAR only, green = wet in aerial photos only).

9. Correspondence between the TerraSAR-X and aerial photograph flood extents over the rural validation area (region B), superimposed on the TerraSAR-X image (blue = wet in SAR and aerial photos, red = wet in SAR only, green = wet in aerial photos only).

10. Possible multi-scale visualisation of flood extents in (a) rural (blue = predicted flood), and (b) urban areas (yellow = predicted flood, brown = shadow/layover areas that may be flooded).

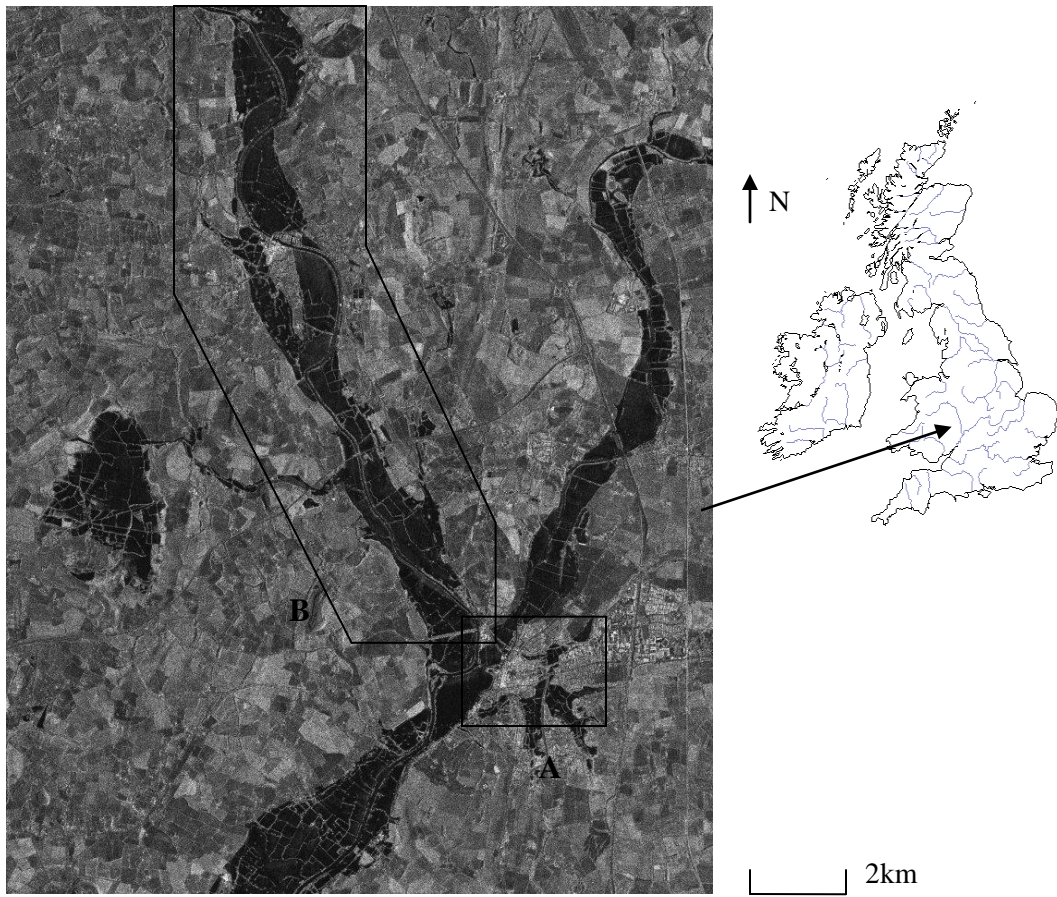


Figure 1.



Figure 2.

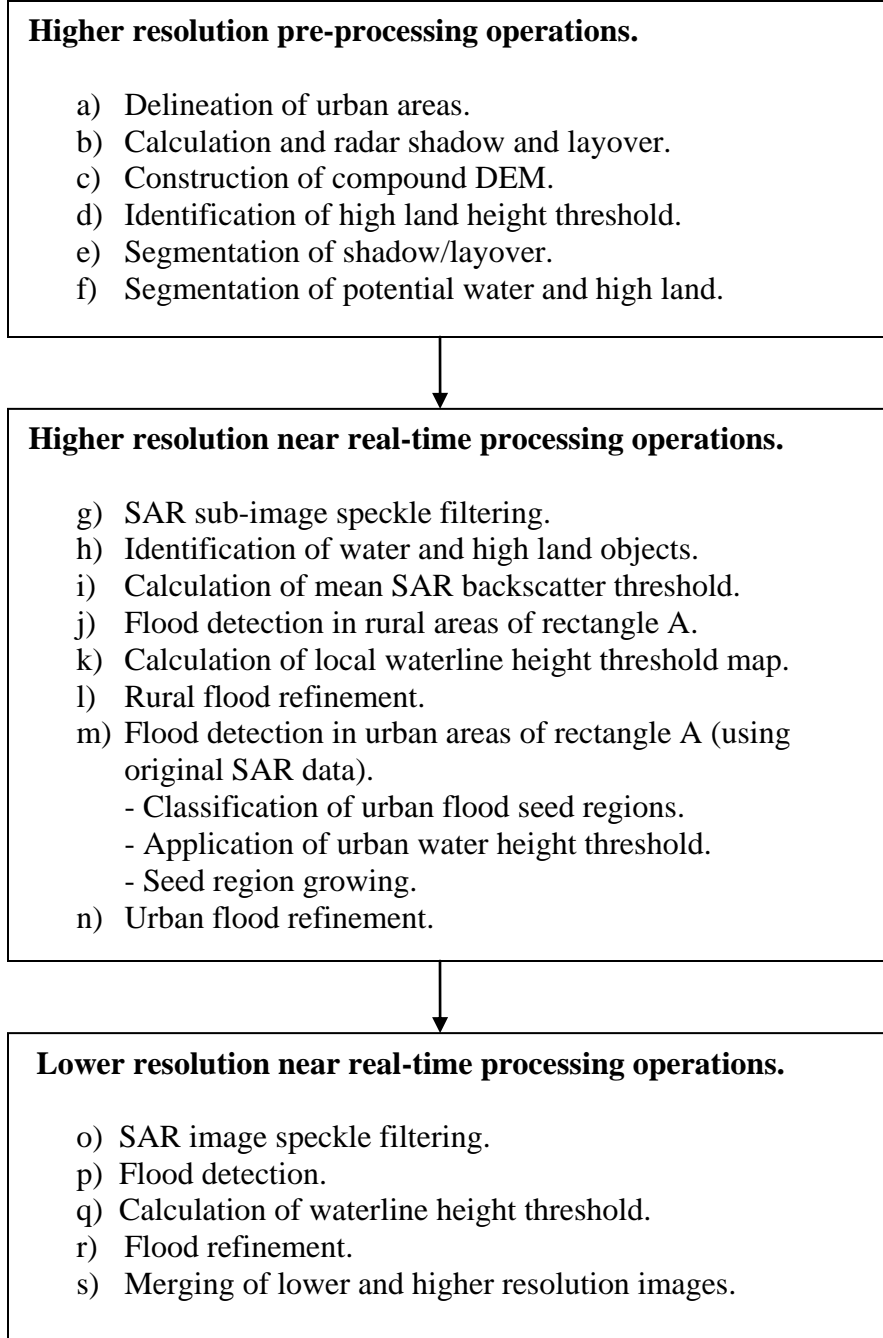


Figure 3.



Figure 4.

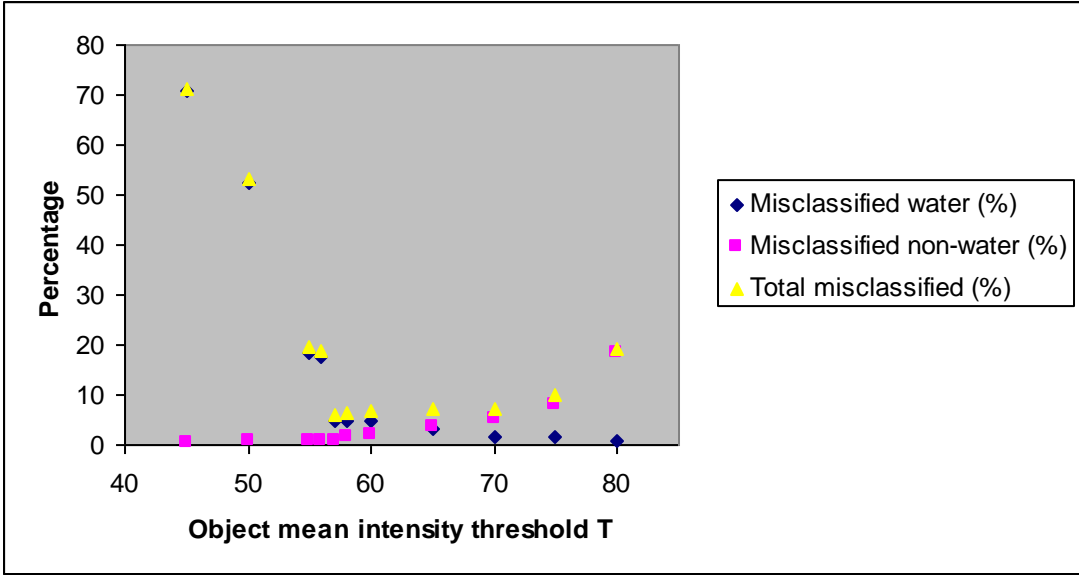


Figure 5.

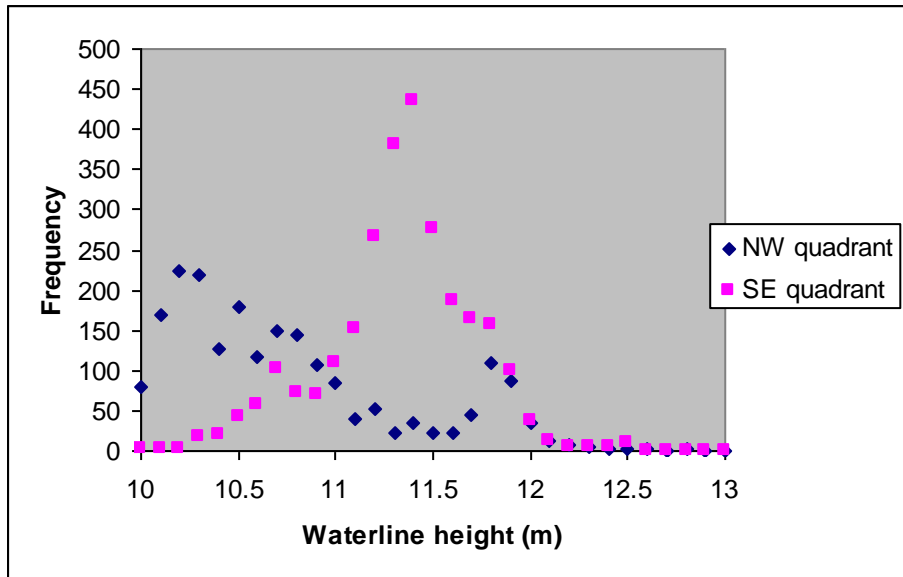


Figure 6.

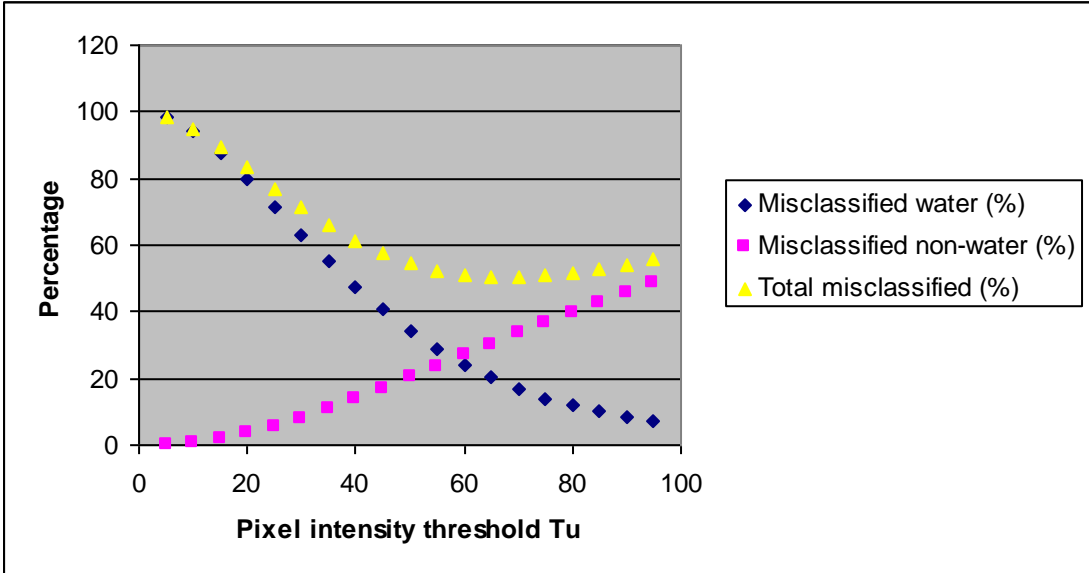


Figure 7.

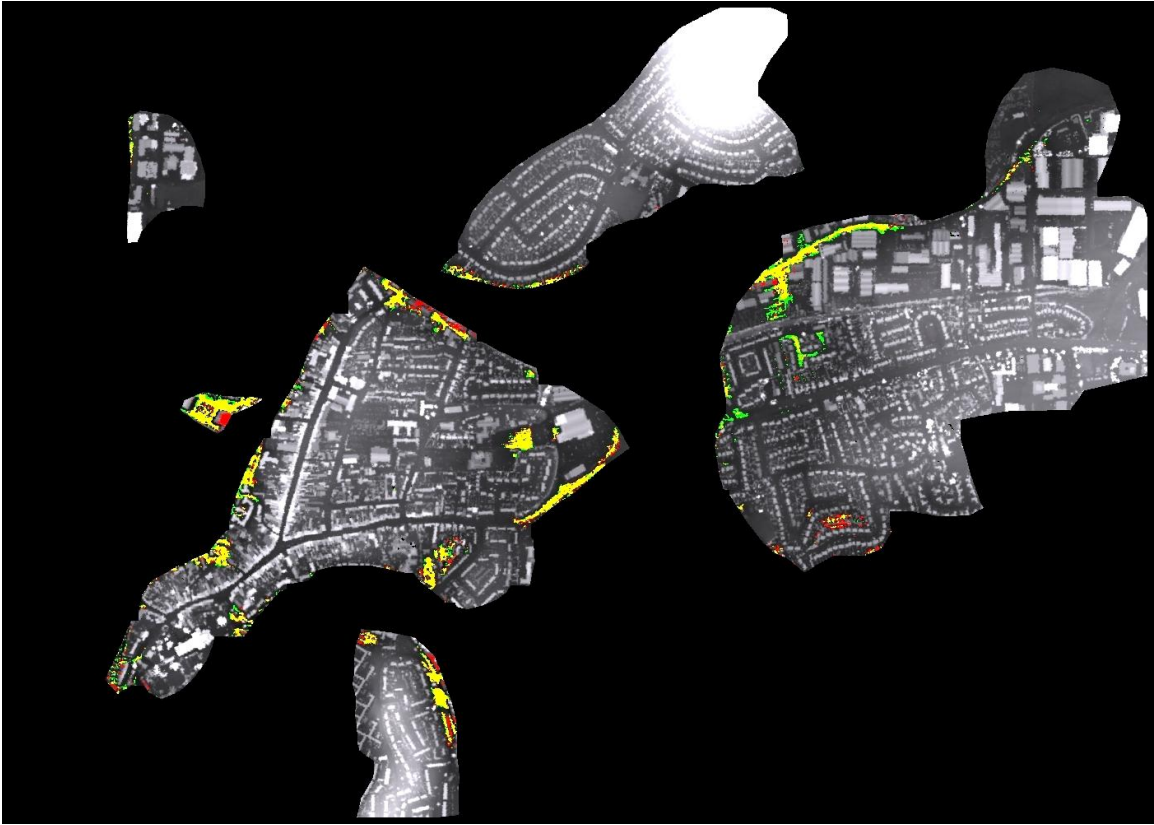


Figure 8.

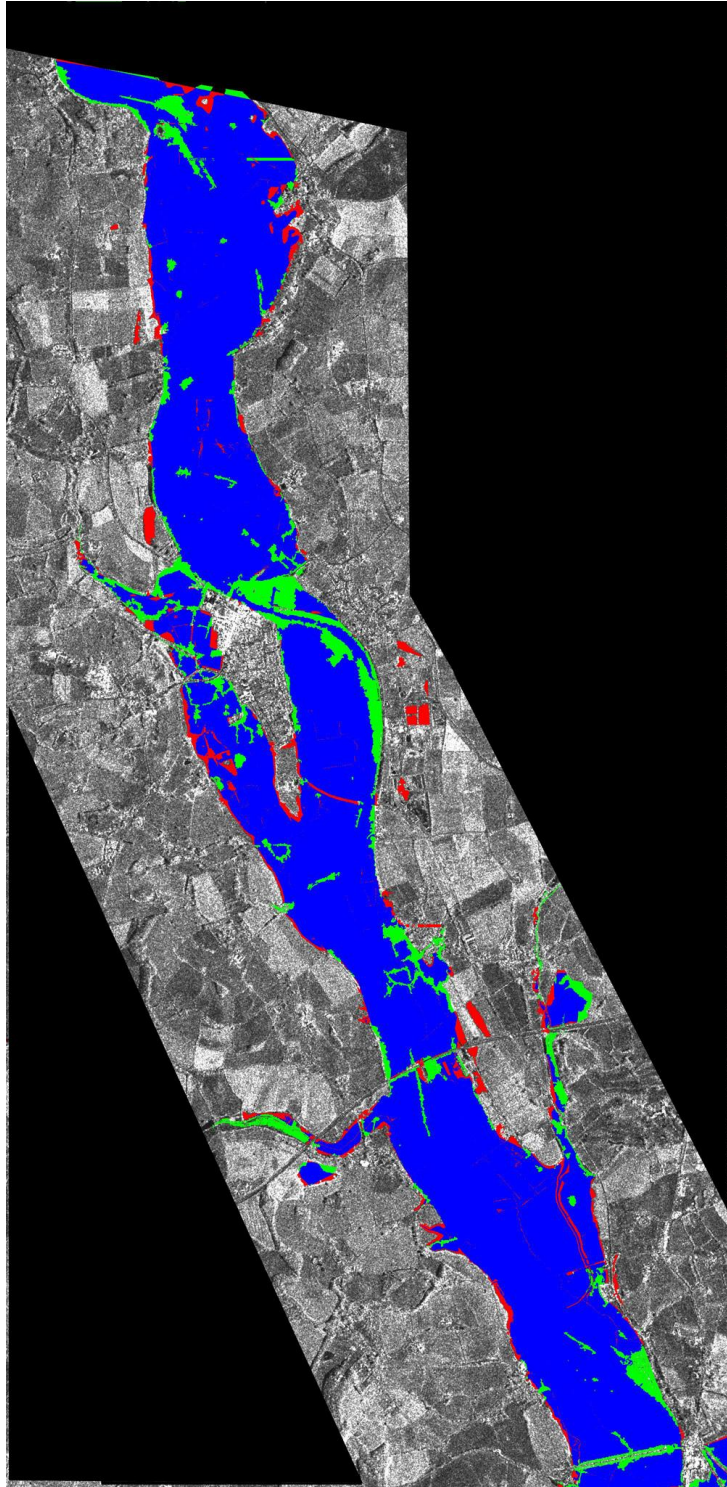
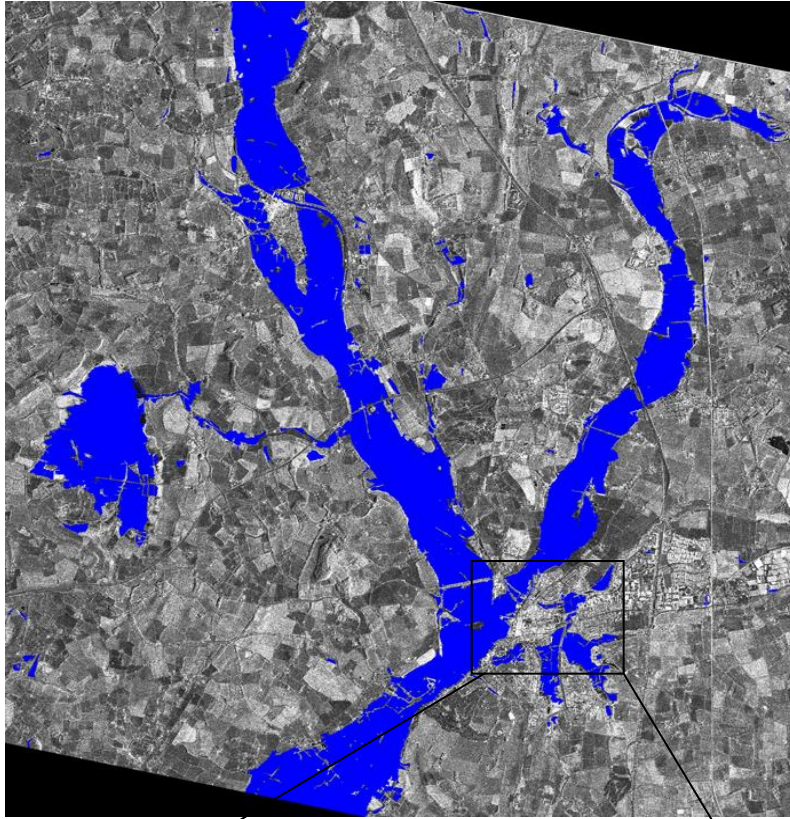
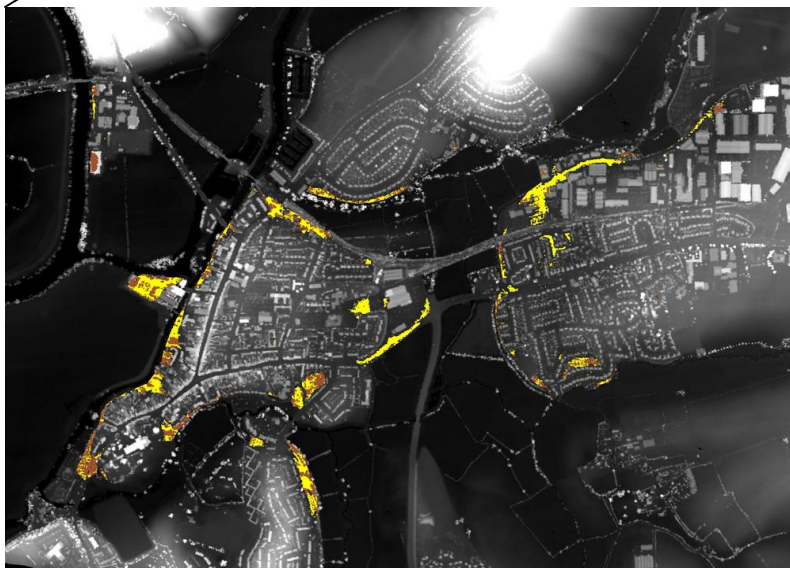


Figure 9.



(a)



(b)

Figure 10.